Controllable synthesis and evolution mechanism of monodispersed Sub-10 nm ZrO$_2$ nanocrystals

Yi Xia[a,b,1], Jie Shi[b,1], Qian Sun[a], Dan Wang[a], Xiao-Fei Zeng[b], Jie-Xin Wang[a,b,*], Jian-Feng Chen[a,b]

[a] Beijing Advanced Innovation Center for Soft Matter Science and Engineering, State Key Laboratory of Organic-Inorganic Composites, Beijing University of Chemical Technology, Beijing 100029, PR China
[b] Research Center of the Ministry of Education for High Gravity Engineering and Technology, Beijing University of Chemical Technology, Beijing 100029, PR China

HIGHLIGHTS

- Monodisperse ZrO$_2$ nanocrystals were controllably prepared by a phase-transfer route.
- The as-prepared ZrO$_2$ nanocrystals have tunable shapes, crystal forms and sizes.
- DFT calculation was used to study the root causes of underpinning growth mechanisms.
- Fluorescent monodispersed ZrO$_2$:Yb^{3+}/Er^{3+} nanocrystals could be similarly prepared.

GRAPHICAL ABSTRACT

ABSTRACT
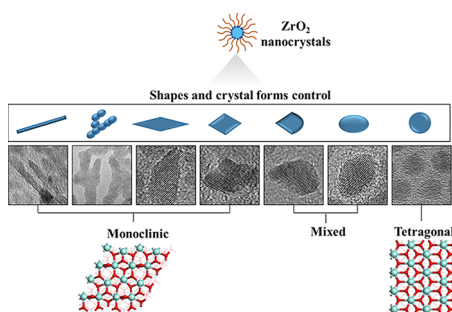
Colloidal nanocrystals can offer exquisite control of physical and chemical properties for technological applications by tuning their sizes, shapes and crystal forms. Herein, a convenient phase-transfer route was presented to controllably prepare transparent dispersions of monodispersed ZrO$_2$ nanocrystals in an aqueous-organic two-phase medium. By adjusting the surfactants, solvents and basicity, the controllability of crystal forms from monoclinic to tetragonal phases, the particle length from 5 to 20 nm, and the different shapes including spindle, cobblestone, sphere, branch, rod and cube can be achieved. The as-prepared ZrO$_2$ nanocrystals can be readily dispersed in nonpolar solvents, thereby forming the ultra-highly concentrated (60 wt%), highly stable (> 18 months) and highly transparent nanodispersions. Density functional theory (DFT) calculations were further used to elucidate the root causes of underpinning growth mechanisms. This work not merely enriches the methodology of controllable fabrication of monodispersed sub-10 nm ZrO$_2$ nanocrystals, but also enables a platform to synthesize rare-earth-doped nanophosphors using ZrO$_2$ as the host matrix. The fluorescent ZrO$_2$:Yb^{3+}/Er^{3+} nanocrystals, which can be easily monodispersed in organic solvents, were also prepared with visible luminescene properties under near-infrared irradiation.

1. Introduction

Exquisite control of colloidal semiconductor nanocrystals has reached a new horizon recently [1–8]. Among them, ZrO_2 is one of the most studies oxides, owing to its high refractive index, high dielectric constant, extremely high hardness, low thermal conductivity, relatively low thermal expansion coefficient and chemical inertness. ZrO_2 exhibits polymorphism including monoclinic, tetragonal and cubic phases. The crystal forms and shapes of ZrO_2 nanoparticles can profoundly affect their physical and chemical properties. From the crystal forms perspective, monoclinic ZrO_2 displays promising catalytic activities, such as in the CO conversion [9,10] and C–H bond dissociation reactions [11,12]. Tetragonal and cubic ZrO_2 are suitable for applications such as dental materials [13,14], refractory materials [15], ferroelectrics [16] and optical coatings [17]. From the view of shapes, spherical ZrO_2 nanocrystals have been applied for phosphate detecting [18], electrode materials [19] and adsorbents [20]. In contrast, ZrO_2 nanocrystals with anisotropic shapes are promising candidates in the fabrication of fibers [21], catalysts [22,23], biomass [24] and grain-oriented ceramics [25,26]. For high solid loaded slurry products, the dispersibility and small size (sub-10 nm) of ZrO_2 nanocrystals are required to enable the research under solution-like conditions and maintain transparency, especially the optical applications [27,28].

Many synthetic routes have been proposed for realizing monodispersed ZrO_2 in the 10 nm size regime, such as non-hydrolytic method in benzyl alcohol [29–32], in situ synthesis method [17], and self-regulating precursors combined with solvothermal method [27,28,33]. However, there are still some challenges related to the raw materials and preparation process. The key drawbacks should be the high cost and moisture sensitivity of the commonly used organic zirconium sources (zirconium propoxide or zirconium butoxide solution). At the same time, the organic surrounding restricts the use of inorganic salts for rare earth doping [34,35]. On the other hand, the synthetic process employing inorganic zirconium sources such as zirconium basic carbonate ($3ZrO_2\cdot CO_2\cdot yH_2O$) or $Zr(CF_3COO)_4$ usually leads to heterogeneous precipitation during the precursor preparation, which may also cause difficulties for equipment cleaning. In addition, crystalline-controlled growth of ZrO_2 nanocrystals has been achieved and proved to be strongly depended on synthesis parameters including surfactants [29,36], solvents [37,38], basicity [39], aging [36] and temperature [38]. However, the fine-tuning of ZrO_2 nanocrystals morphology has been rarely documented, especially for one-dimensional ZrO_2 nanostructures (rods, wires, and tubes). The most accepted growth process for shape-control is known as "oriented attachment", which suggests that the ultimate shape determination is induced by the relative surface energy difference of each facet of the crystal [40–42]. There have been reported numbers of shape-control nanomaterials focusing on metals [42], sulfides [43], selenides [44–46], or other semiconductor metal oxides such as TiO_2 [47], CeO_2 [48], Fe_3O_4 [49] or ZnO [50], whereas ZrO_2 systems remain poorly explored. Therefore, to extend the technological potential of ZrO_2, it is very necessary and desired to develop a cost-effective and eco-friendly method for the preparation of ZrO_2 nanocrystals with tunable crystal forms, shapes, sizes and dispersibility.

In this work, a convenient phase-transfer approach is proposed for the synthesis of monodispersed ZrO_2 nanocrystals with tunable crystal forms and morphologies. The as-prepared ZrO_2 nanocrystals can be readily dispersed in nonpolar solvents, thereby forming ultra-highly concentrated (60 wt%), highly stable (> 18 months) and highly transparent nanodispersions. Since water is an ideal solvent for inorganic species, and long-chain fatty acids in organic phase serve as surfactants to render the nanoparticles dispersible in nonpolar solvents, hydrophilic $Zr(OH)_4$ precursor can be transformed to hydrophobic ZrO_2 nanocrystals by a hydro/solvothermal process in water–oil dual phases. In this case, zirconium oxychloride, as one of the most inexpensive inorganic zirconium sources, is employed to form stable precursor in homogeneous aqueous phase. The ratio of tetragonal and monoclinic in

mixed-phase ZrO_2 nanocrystals can be effectively tuned by adjusting the length of surfactants without using any dopant or supported species, while achieving the tuning of shape and particle length. In addition, the solvent and basicity are closely tied to the shape of ZrO_2 nanocrystals, especially for the elongated morphologies, which may lead encouraging epitaxial growth along a longitudinal direction. The further DFT calculations indicate that the significant difference of adhesion energies between covering ligands and various crystallographic planes is the fundamental cause of anisotropic growth. Furthermore, this approach was also successfully applied to the preparation of fluorescent ZrO_2:Yb^{3+}/Er^{3+} nanocrystals in ZrO_2-based nanocrystals, which have gained attentions on the consequential crystal forms [51], morphology [18] and optical properties [52] for potential applications, such as photodynamic therapy [53], photodetectors [54] and near-infrared sensing [55].

2. Experimental section

2.1. Chemicals

Zirconium oxychloride octahydrate ($ZrOCl_2\cdot 8H_2O$), ytterbium nitrate hexahydrate ($Tb(NO_3)_3\cdot 6H_2O$), erbium nitrate hexahydrate ($Er(NO_3)_3\cdot 6H_2O$), sodium hydroxide (NaOH), acetone, alcohol, benzyl alcohol, n-heptane (n-C_7H_{16}), n-decane (n-$C_{10}H_{22}$), cyclohexane (CYH), toluene, tetrahydrofuran (THF), chloroform ($CHCl_3$), petroleum ether (boiling range: 60–90 °C) (MSO), decanoic acid (C10), dodecanoic acid (C12), myristic acid (C14), stearic acid (C18) and docosanoic acid (C22) were purchased from Aladdin Bio-Chem Technology Co.. All solvents used were ACS grade. Deionized water was provided by a water purification system (RO-DI plus, Hitech, PRC).

2.2. Preparation of aqueous $Zr(OH)_4$ precursor

Aqueous $Zr(OH)_4$ precursor was synthesized according to the procedure described elsewhere [38]. 2.0946 g (6.5 mmol) of $ZrOCl_2\cdot 8H_2O$ was dissolved in 65 mL of deionized water at 25 °C under vigorous stirring. 38 mL of aqueous solution containing 0.19 g of NaOH (0.125 mol/L) was then dropwise added into the above $ZrOCl_2$ aqueous solution. The as-obtained zirconium hydroxide precursor had a pH value of about 2, and was further stirred at 70 °C for 3 h. Subsequently, it was washed thoroughly with deionized water by a dialysis method.

The concentration of NaOH solution can be changed to 0.375 mol/L (38 mL of aqueous solution containing 0.57 g of NaOH). In this case, the pH of the as-obtained precursor was around 4. Afterwards, the precursor was further washed three times with water using centrifugation at 5000 rpm for 5 min to remove the inorganic ions. It deserves to be mentioned that the washing process (dialysis or centrifugation) is essential for the monodispersity of ZrO_2 nanodispersion, since the residual inorganic salt ions in the precursor can lead to the formation of clusters [56,57], as shown in Fig. S1.
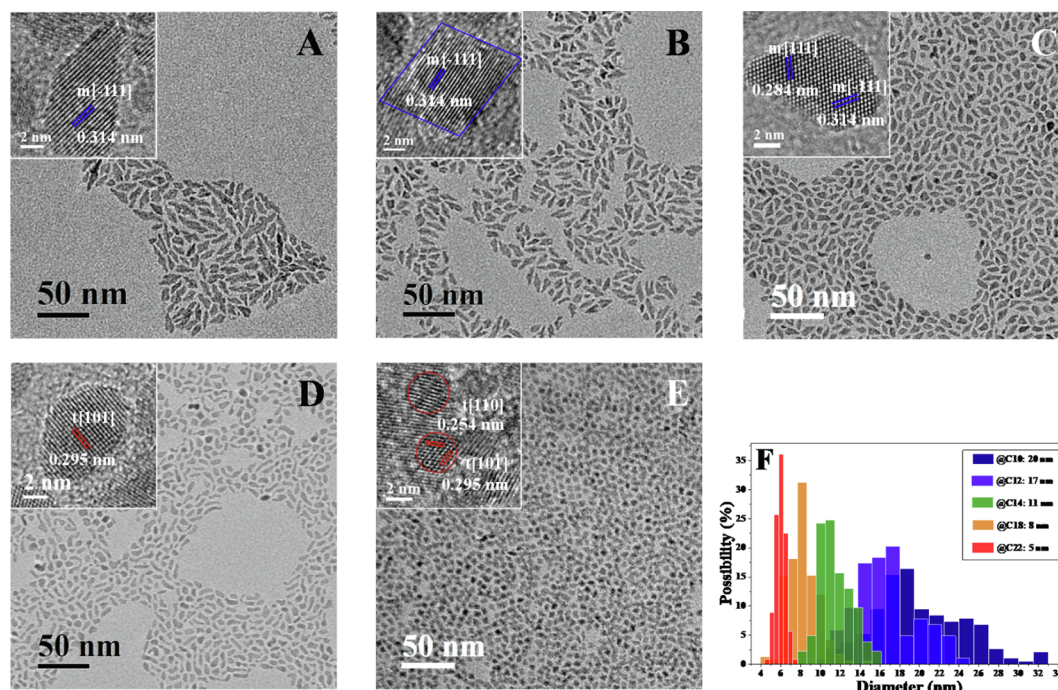
2.3. Synthesis of monodispersed ZrO_2 nanocrystals and rare-earth doped ZrO_2 nanocrystals

1.2 g of fatty acid (C10, C12, C14, C18 or C22) was dissolved in 16 mL benzyl alcohol. The formed solution was added into 38 mL aqueous zirconium hydroxide precursor. The mixture was further transferred into a 200 mL Teflon-lined stainlesssteel autoclave and heated at 210 °C for 48 h. After cooling down, the benzyl alcohol-water–solid mixture was separated by using centrifugation at 5000 rpm for 5 min. The white ZrO_2 solids were washed three times using ethanol to remove the excessive alkyl acid and solvent. The product can be redispersed in nonpolar solvents, including n-C_7H_{16}, n-$C_{10}H_{22}$, CYH, toluene, THF, $CHCl_3$, white oil and petroleum ether (boiling range: 60–90 °C), to form a clear 'solution'.

When benzyl alcohol was replaced with nonpolar solvents such as n-
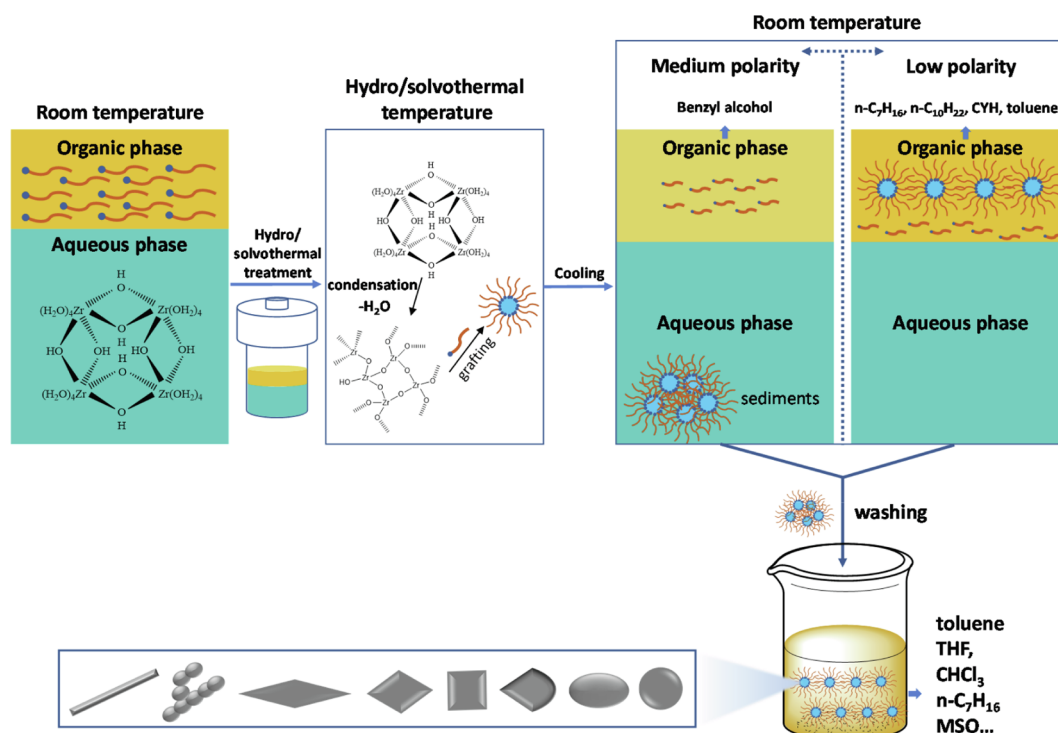
Scheme 1. Schematic diagram for the possible formation mechanism of monodispersed ZrO_2 nanocrystals prepared in the benzyl alcohol-water system and n-C_7H_{16}-water system.
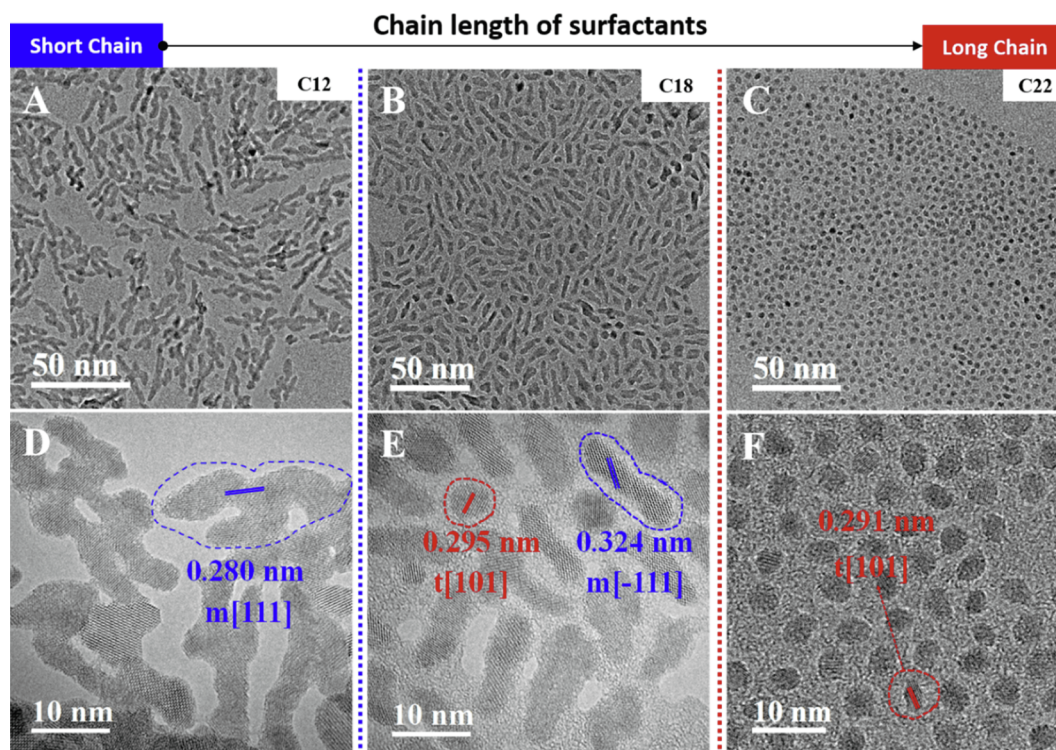

Fig. 1. TEM and HRTEM images of monodispersed ZrO_2 nanocrystals prepared with C10 (A), C12 (B), C14 (C), C18 (D), C22 (E) modification in the benzyl alcohol-water system; and the corresponding particle size distributions (E) (for each histogram, over 100 particles were measured).

C_7H_{16}, n-$C_{10}H_{22}$, CYH or toluene, the difference was that ZrO_2 nano-crystals can be monodispersed in organic phase instead of precipitating out as powders (Scheme 1). After cooling down, the n-C_7H_{16} (n-$C_{10}H_{22}$, CYH or toluene)-water–solid mixture was separated using centrifuga-tion at 5000 rpm for 5 min. Excess acetone was added to the organic phase to precipitate the white product, which was collected by cen-trifugation and further washed twice by ethanol to remove the

excessive alkyl acid and solvent. The final product can be re-dispersed in the above-mentioned nonpolar solvents.

For the preparation of ZrO_2:Yb^{3+}/Er^{3+} nanocrystals, 12 mol% of Yb $(NO_3)_3$·$6H_2O$ and 2.4 mol% of Er$(NO_3)_3$·$6H_2O$ with respect to zirconia, were dissolved in the Zr$(OH)_4$ precursor. The other processes are same as the above description.

Fig. 2. TEM and HRTEM images of monodispersed ZrO_2 nanocrystals with C12 (A), C18 (B), C22 (C) modification; and the corresponding HRTEM images of ZrO_2 nanocrystals prepared with C12 (D), C18 (E), C22 (F) modification in the n-C_7H_{16}-water system.
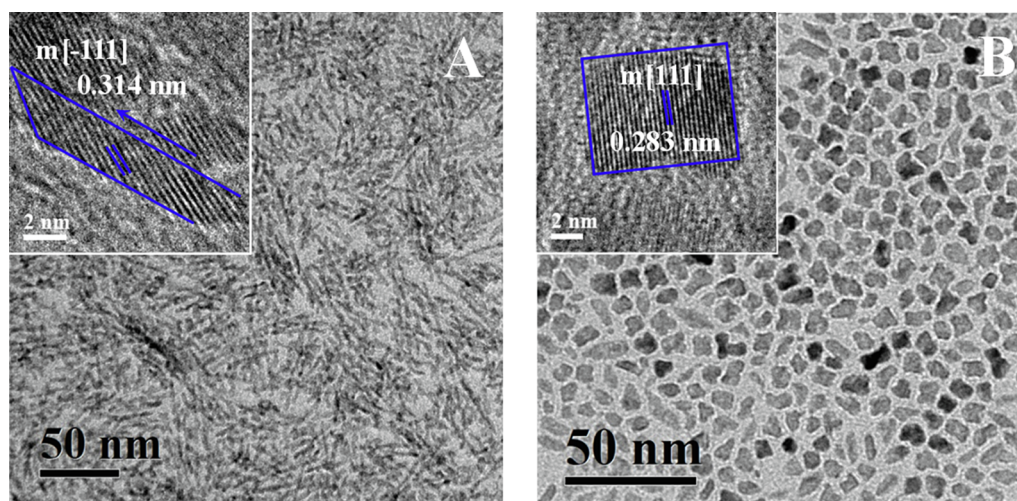
Fig. 3. TEM and HRTEM images of ZrO_2 nanocrystals prepared with C12 modification and NaOH concentration of 0.375 mol/L in the n-C_7H_{16}-water system (A); and with C12 modification and NaOH concentration of 0 mol/L in the benzyl alcohol-water system (B).

Table 1
Adsorption energies (eV) of COO^- and COOH adsorbed on {−1 1 1}, {1 1 1}, {0 0 2} and {0 2 2} planes of monoclinic ZrO_2.

Structures	Facets			
	{−1 1 1}	{1 1 1}	{0 0 2}	{0 2 2}
COOad1	−0.96	−0.90	−1.82	−2.48
COOad2	−1.30	−1.09	−1.27	−2.07
COOHad1	−0.72	−1.66	−2.19	−2.73
COOHad2	−0.87	−0.67	−2.19	−0.89

2.4. Computational models and methods

Zr atoms are eight-coordinated in tetragonal phase, whereas they are seven- coordinated in the monoclinic phase. {−1 1 1} and {1 0 1} planes of monoclinic and tetragonal ZrO_2, respectively, are employed because they are the most stable [58]. Considering the complicacy of surfactants, long carbon chain was truncated to a simplified methyl group (–CH$_3$) to investigate the adsorption characters on ZrO_2 facets [59,60]. We modeled the interactions between the COO^- and COOH molecules and the facets severally under two possible adsorption configurations: named as COOad1/COOad2 for COO^- adsorption conditions and COOHad1/COOHad2 for COOH adsorption conditions. The adsorption energy was determined by:
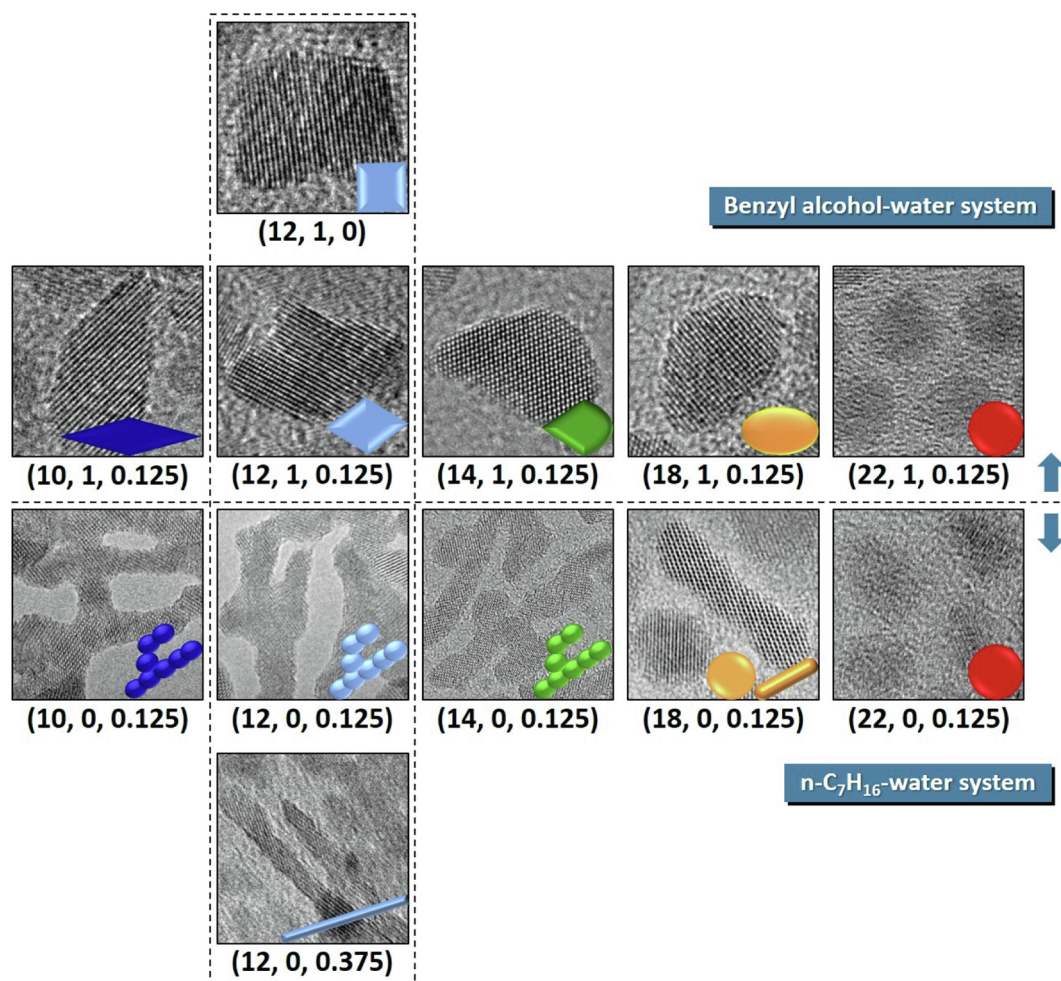
Fig. 4. TEM overview of ZrO$_2$ nanocrystals with different shapes. The three digital condition codes (X, Y, Z) represent different reaction conditions where: X = 10, represents the capping agent was C10, and so on; Y = 1, where the nanocrystals were prepared in the benzyl alcohol-water system; Y = 0, where the nanocrystals were prepared in the n-C$_7$H$_{16}$-water system; Z = 0, indicates the concentration of NaOH solution used in precursor preparation process was 0 mol/L, and so on.

$$E_{adsorption} = E_{total} - E_{slab} - E_{adsorbate}$$

where the E_{total} is the energy of the adsorption complex including the crystal slab and adsorbate molecules, E_{slab} is the total energy of the crystal slab, and $E_{adsorbate}$ is the energy of the isolated adsorbate molecule or atom.

Density functional theory (DFT) calculations with spin-unrestricted in this work were done by Vienna ab initio simulation package (VASP.5.4.1) [61]. The re-parameterized form of Perdew-Burke-Ernzerhof (revPBE) functional with the generalized gradient approximation (GGA), was used to calculate non-local gradient corrections to the correlation and exchange energies [62,63]. The wave functions projected in real space were constructed from the expansion of plane waves with an energy cutoff of 450 eV. A $4 \times 4 \times 1$ Gamma centered Monkhorst-Pack k-point sampling in the surface Brillouin zone was performed for the surfaces, and a vacuum layer of 20 Å was set to avoid interactions between the periodic slabs. Geometry optimizations were performed using a 4-layer ZrO$_2$ model of 16 Zr atoms and 32O atoms, with the bottom two layers being fixed. The structural optimizations were carried out at a tight convergence of 0.01 eV/Å on the forces with the wave functions converged to 1×10^{-5} eV. In order to accurately describe the dispersion interactions between the adsorbate and the surface, all calculations were performed using the Rutgers-Chalmers van der Waals Density Functional (vdw-DF) method [64].

2.5. Characterization

The size and morphology of ZrO$_2$ nanocrystals were examined with a transmission electron microscope (TEM) (H-9500, HITACHI, Japan) operating at an accelerating voltage of 300 KV. Crystalline structure of ZrO$_2$ nanocrystals was performed by an X-ray diffractometer (XRD-6000, Shimadzu, Japan) equipped with CuKa radiation, at an accelerating voltage of 40 kV and a current of 40 mA. The scanning range was from 10° to 80°, and the scanning rate was 5°/min with a step size of 0.02°. Fourier transform IR (FTIR) spectrum was recorded with a Nicolet 6700 spectrometer (Nicolet Instrument Co., USA) in the range of 4000–400 cm^{-1}. Thermogravimetric analysis (TG) was performed on Netzsch TG (SDT Q600 V20.9 Build 20) at a scanning rate of 10 K/min under a nitrogen atmosphere. Upconversion luminescence spectrum of the sample was acquired on a Maestro *in vivo* optical imaging system (CRI, Inc. Woburn, MA) equipped with a commercial 980 nm laser.

3. Results and discussion

Fig. 1 shows the representative TEM, HRTEM images of monodispersed ZrO$_2$ nanocrystals obtained in the benzyl alcohol-water system with the addition of different fatty acids (C10–C22), and the corresponding particle size distributions. The nanocrystals appear rather well spaced because of the fatty acids coating. Moreover, the nature of the capping agent plays an important role in controlling the
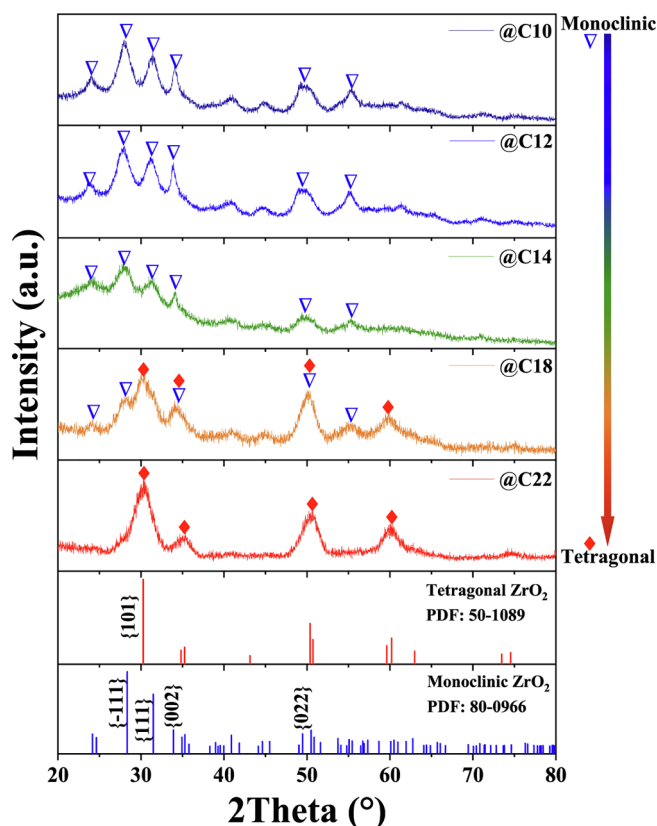
Fig. 5. XRD patterns of ZrO_2 nanocrystals prepared with C10, C12, C14, C18, and C22 modification in the $n\text{-}C_7H_{16}$-water system.

Fig. 6. (A) FTIR spectra of C12, and ZrO_2 nanocrystals modified by C12 (ZrO_2@C12); (B) TG curve and the corresponding derivative TG curve of ZrO_2 nanocrystals prepared with C12 modification in the $n\text{-}C_7H_{16}$-water system.

shape of the ZrO_2 nanocrystals. The samples functionalized with C10 and C12 exhibit roughly spindle shapes. When the ligand length increases from C14 to C22, the ZrO_2 nanocrystals gradually tend to be smooth and round. The HRTEM images (the insets in Fig. 1A–E) show the isolated crystal and morphological nature of such nanoparticles. It appears that the shape of ZrO_2 nanocrystals@C14 is a transition from fusiform shape (ZrO_2 nanocrystals@C12 in Fig. 1B) to cobblestone-like shape (ZrO_2 nanocrystals@C18 in Fig. 1D). The longer hydrocarbon chain of fatty acids, the less elongated ZrO_2 nanoparticles are formed, and the more uniform particle distributions can also be obtained, which is shown in Fig. 1F. Because of steric hindrance, longer chain ligands are less mobile and reactive than their shorter chain counterparts [65], consequently, anisotropic growth is suppressed. In addition, the clear lattice indicates the high crystallinity of the as-synthesized nanoparticles. The lattice space of 0.314 nm and 0.284 nm in Fig. 1(A–C) correspond to $\{-1\,1\,1\}$ and $\{1\,1\,1\}$ planes of monoclinic ZrO_2 structure, respectively, while the lattice space of 0.295 nm and 0.254 nm in Fig. 1(D, E) correspond to the $\{1\,0\,1\}$ and $\{1\,1\,0\}$ plane of tetragonal ZrO_2 structure. The results demonstrate that the concurrent crystalline form transition occurred in the obtained ZrO_2 nanocrystals when the chain ligand changed in hydro/solvothermal process. Therefore, we consider that organic surfactants have a key role in determining not only the shape and size, but also the crystalline form of the products.

Fig. 2 shows the representative TEM, HRTEM images of monodispersed ZrO_2 nanocrystals obtained in the $n\text{-}C_7H_{16}$-water system with the addition of different long chain fatty acids (C12, C18 and C22). In this case, the benzyl alcohol was replaced with $n\text{-}C_7H_{16}$. The morphology of ZrO_2 nanocrystals was significantly changed from spindle-like shape in the benzyl alcohol-water system to irregular branch structure in the $n\text{-}C_7H_{16}$-water system, when using the same C12 as capping agents. The HRTEM image in Fig. 2E demonstrates that monoclinic ZrO_2 nanoparticles have the tendency to link in a head-to-head manner to form nanorods. Therefore, a proposition is employed to
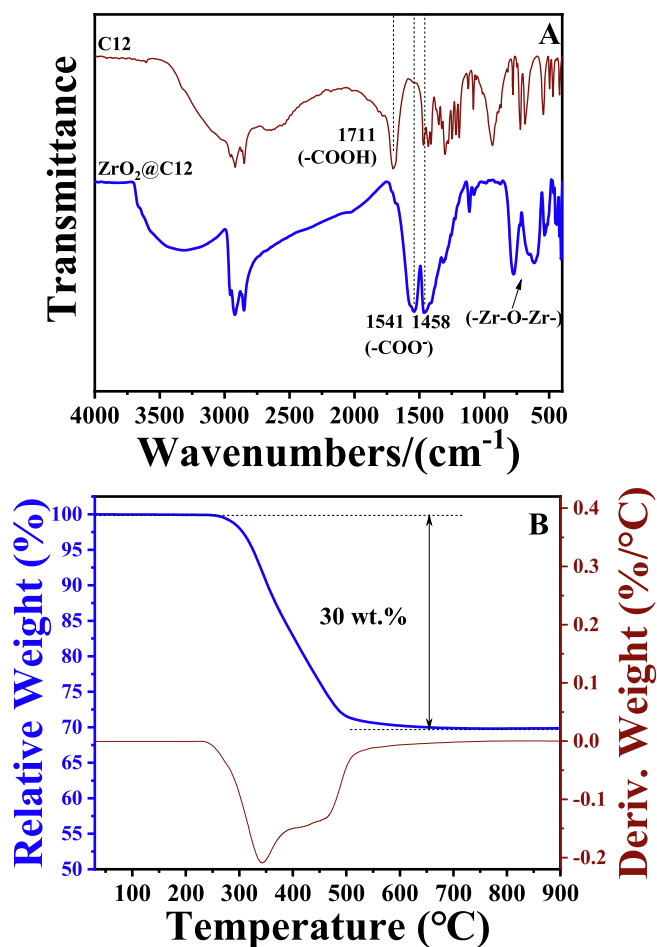
account for this phenomenon, which relies on the immiscibility of $n\text{-}C_7H_{16}$ with water. The water-solubility of organic phase is responsible for the diffusion rate in the organic–inorganic interface between hydrophilic precursor and oleophilic surfactants. To examine this proposition, the experiments were carried out in which $n\text{-}C_7H_{16}$ was substituted with $n\text{-}C_{10}H_{22}$ (chain hydrocarbon), CYH (cycloalkane) and toluene (aromatic hydrocarbon) as the solvents in organic phase, and the corresponding TEM images are displayed in Fig. S2. By applying these three water-immiscible organic solvents, the ZrO_2 nanocrystals exhibit a similar morphology and connecting features regardless of solvents structure. Since $n\text{-}C_7H_{16}$ (or $n\text{-}C_{10}H_{22}$, CYH, toluene) is more hydrophobic than benzyl alcohol, we believe that there are not abundant surfactants exchanging on the surface of nanoparticles during crystal growth, according to the concept of dynamic solvation [65]. In addition, surfactant-controlled growth also happened in the ZrO_2 nanocrystals obtained in the $n\text{-}C_7H_{16}$-water system. C10 and C14 capped ZrO_2 nanocrystals display a similar fashion with C12 capped ZrO_2 nanocrystals, which are shown in Fig. S3. The branched nanocrystals with monoclinic phase were replaced by nanorods. Meanwhile, spherical particles with tetragonal phase occurred, when the hydrocarbon chain length of surfactant increased to C18 (Fig. 2B and E). The ZrO_2 nanocrystals covered with C22 were predominantly the spherical morphology form and tetragonal phase (Fig. 2C and F).

The precursor is also a key factor for shape controlling. We changed the extent of precursor hydrolyzation by tuning the concentration of NaOH solution from 0.125 to 0.375 mol/L, while keeping all the other preparative conditions constant. As shown in Figs. 2A and 3A, the shape
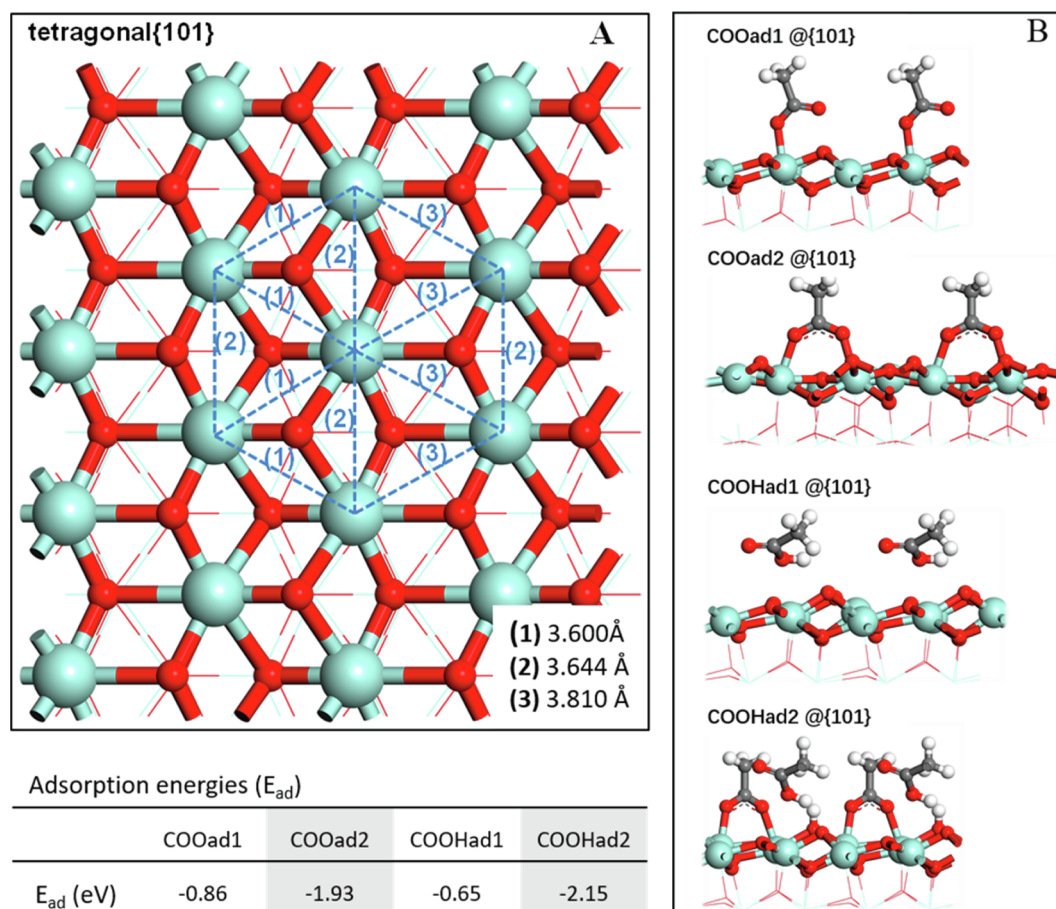
Fig. 7. (A) Ball-and-stick models of the crystalline structure of tetragonal ZrO_2 facets: top view of {1 0 1} planes and the corresponding Zr-Zr distances (unit: Å); (B) adsorption models of COO^- and $COOH$ ligands on {1 0 1} planes with different initial configurations; and the adsorption energies (eV) of CH_3COO^- and CH_3COOH adsorbed on {1 0 1} planes. The color of the atoms are: Zr atoms: blue and O atoms: red.

of nanocrystals changed from branched nanostructures to nanorods with higher length-diameter ratio. In the regime of shape control, the competition relationship between crystallization and capping process is the key factor: capping dominance can stabilize precursors, whereas rapid crystallization causing particular crystal facets de-capping can initiate anisotropic growth of nanocrystals. We believe that a higher alkali source concentration can produce larger prenucleation clusters. This renders relatively rapid crystallization process, and leads to the appearance of elongated shapes. Analogously, insufficient capping caused by solvent solubility also can initiate selectively adhering to crystal facets. Consequently, the ZrO_2 nanocrystals obtained in the n-C_7H_{16}-water system (Fig. 2A) show more elongated morphologies than that in the benzyl alcohol-water system (Fig. 1B). To validate this proposition, an additional synthesis was performed in which the concentration of NaOH solution was decreased to 0 mol/L in the benzyl alcohol-water system. As displayed in Fig. 3B, the ZrO_2 nanocrystals produced in relatively slow crystallization and sufficient capping process predominantly show cube-like shape with low length-diameter ratio, which corresponded to the proposed shape-control regime.

A comprehending of how facets of a nanocrystal develop, and surfactants preferentially adsorb on which surface is critical for interpreting nanocrystal shape. We evaluated the interaction between the surfactants, and { −1 1 1}, {1 1 1}, {0 0 2} and {0 2 2} planes of monoclinic ZrO_2 by the first-principle calculation based on the DFT. Computation models of these four facets and the corresponding Zr-Zr distances are displayed in Fig. S4. The carboxylates in the ligands have a strong binding affinity to Zr atoms at the surface either in monodentate or bidentate configurations [66] (Figs. S5–S8). The adsorption

energies of COO^- and $COOH$ on the { −1 1 1}, {1 1 1}, {0 0 2} and {0 2 2} planes are shown in Table 1. As these calculations indicates, the adsorption energies of ligands on { −1 1 1} and {1 1 1} facets (∼-1.0 eV) are overwhelmingly smaller than that on other facets (∼-2.0 eV). The binding preference suggests a much weaker binding to { −1 1 1} and {1 1 1} facets, thus the growth of ZrO_2 nanocrystals will occur more rapidly on { −1 1 1} and {1 1 1} facets than other facets in incomplete coverage situation. In addition, total energies in Table S1 suggest that { −1 1 1} and {1 1 1} facets are comparably more energetically stable than the other two, finally leading to the dominant surfaces of the crystal. Fast-growing facets will not be easily terminated by surfactants during the growth, resulting in an anisotropic growth regime. This accounts for why the obtained ZrO_2 nanocrystals in the n-C_7H_{16}-water system show an elongated morphology and grew around { −1 1 1} and {1 1 1} crystal orientation (Figs. 2D, E and 3A).

Fig. 4 outlines an array of ZrO_2 nanocrystals synthesized using regulating specific fatty acids, organic solvents and NaOH concentration. The shape change is the result of both the surfactants and the diffusion mechanism [65], which are reflected at the three factors listed in the diagram. As mentioned above, the water-solubility of organic solvents and NaOH concentration adjust the diffusion rate of surfactants into the reactive crystal facets and the nucleation rate of precursors, respectively. Longitudinally, the framed column demonstrates that lower diffusion rate and higher nucleation rate can promote the epitaxial growth around specific facets, causing nanocrystals with higher length-diameter ratio. Synchronically, the surfactant with the longer carbon chain is more beneficial to the generation of round-shaped nanocrystals owing to the random and uniformly distributed spatial steric
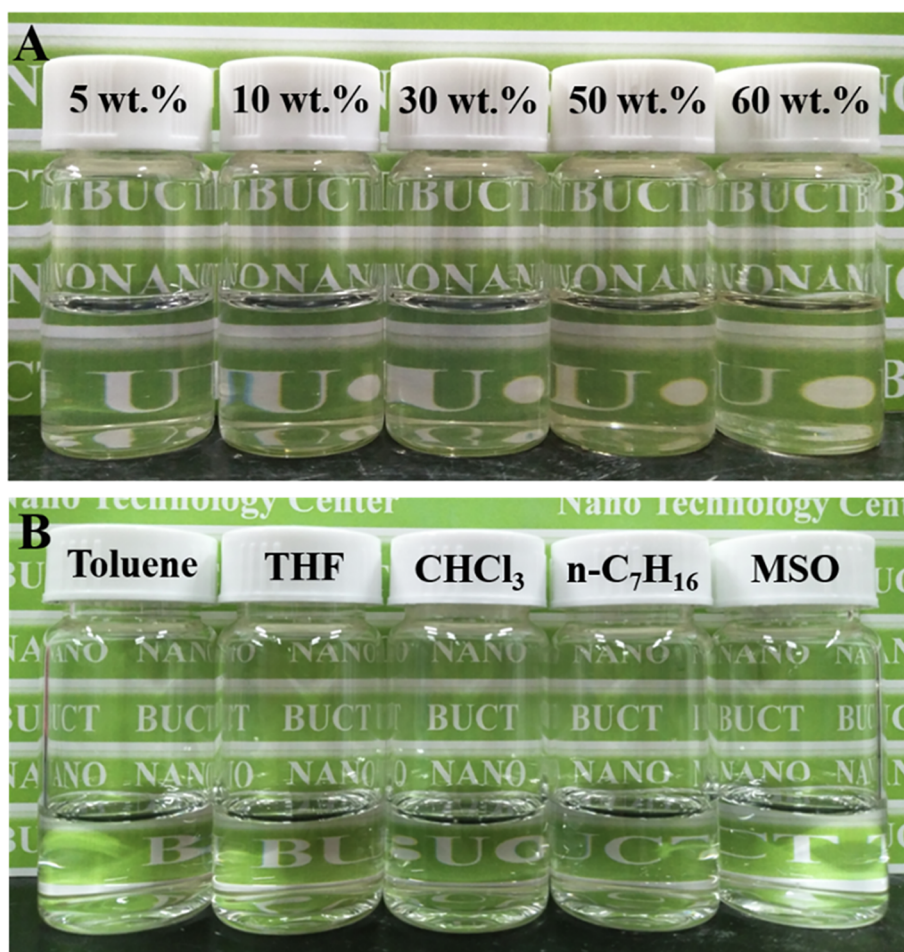
Fig. 8. Digital photographs of ZrO$_2$ nanodispersions with different solid contents and the same solvent CYH (A); and ZrO$_2$ nanodispersions with the same solid content of 1 wt% and different solvents (B).

hindrance at all directions. This work presents a logically controlled fabrication of one-dimensional sub-10 nm monodispersed ZrO$_2$ nanocrystals programmed by the combinational conditions of surfactants, solvents and raw materials.

Fig. 5 exhibits the XRD patterns of ZrO$_2$ nanocrystals capped with varying fatty acids in the n-C$_7$H$_{16}$-water system. Definitely, longer hydrocarbon chain of fatty acids favors the formation of tetragonal ZrO$_2$ phase, which is in good agreement with the crystalline change regulation reported previously [36,67]. C10, C12 and C14-capped ZrO$_2$ nanocrystals were the pure monoclinic phase form, whereas C18-capped ZrO$_2$ nanocrystals were a mixture of monoclinic and tetragonal phases, which was in close accordance with the TEM data in Fig. 2. In the terminal stage, pure tetragonal ZrO$_2$ nanocrystals were obtained when the ligand length was up to C22. The XRD patterns of ZrO$_2$ nanocrystals obtained in the benzyl alcohol-water system are similar to the counterparts except for the C14-capped ZrO$_2$ nanocrystals, which are displayed in Fig. S9. The difference is the remarkable occurrence of tetragonal phase in semi-round and semi-fusiform shaped ZrO$_2$ nanocrystals@C14 (Fig. 1C). These results prove that the round morphology is closely tied to tetragonal phase, whereas clubbed and cuspidal morphology is related to monoclinic phase of ZrO$_2$ nanocrystals.

The interaction between ZrO$_2$ nanocrystals and capping agents was confirmed by the FTIR spectra and TG curve (Fig. 6). As shown in Fig. 6A, the strong bands in the range of 600–700 cm^{-1} were the -Zr-O-Zr- vibration mode. The bands in the 2800–2960 cm^{-1} region were attributed to the C–H stretching mode of methyl and methylene groups. Repeated washing confirms the expelling of unconjugated carboxylic ligands from the ZrO$_2$ surface after the surface modification. Thus, it

deserves to be noticed that the characteristic carboxy group (-COOH) which peaks at 1711 cm^{-1} was not observable in the spectrum of the ZrO$_2$ nanocrystals @C12. Instead, the stretching frequency peaks of the carboxylate group (-COO-) at 1541 and 1458 cm^{-1} took over the place, which suggests that the carboxylate group from C12 was chemically bonded to the surface of ZrO$_2$ nanocrystals [68,69]. Similar FTIR spectra were obtained in ZrO$_2$ nanocrystals capped with C10, C14 and C18, as shown in Fig. S10. The amount of C12 capping the surface of ZrO$_2$ nanocrystals was recorded by the TG curve (Fig. 6B). C12 attached to nanoparticles was broken down completely at around 500 °C, at which nanocrystals underwent an obvious weight loss. The fatty acids coating of 30 wt% was enough to achieve stabilization of around 10 nm particles in organic solvents [70,71]. Since it is challenging to thoroughly remove the surfactant C22 due to the insolubility in ethanol at room temperature, the TG and FTIR tests make no sense for ZrO$_2$@C22. The amount of other fatty acids, including C10, C14 and C18 capping the surface of ZrO$_2$ nanocrystals, was also recorded by TG curves (Fig. S11). Ligands bounded to the nanocrystals are around 30 wt% for C10, C12, C14, and around 27 wt% for C18. Coincidentally, ZrO$_2$@C10, C12 and C14 are monoclinic phase whereas there is tetragonal phase in ZrO$_2$@C18, as shown in Fig. 5. It seems that compared with the tetragonal phase, the monoclinic ZrO$_2$ requires more surfactants for its stability.

To further compare the surface coordination chemistry between the two crystal forms of ZrO$_2$ nanocrystals, DFT calculations of the interaction between ligands and planes of tetragonal ZrO$_2$ were also performed. As shown in Figs. 7A and S4A, it should be noted that {1 0 1} planes of tetragonal ZrO$_2$ nanocrystals (t{1 0 1}) are more symmetry
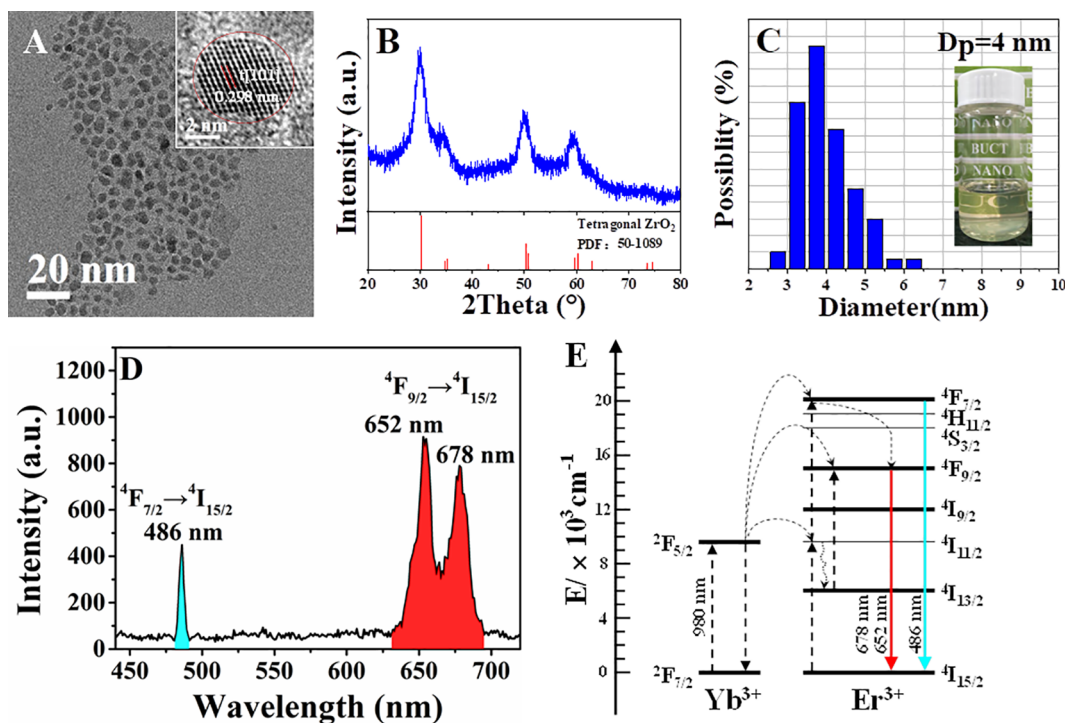
Fig. 9. TEM and HRTEM images (A), XRD pattern (B), the corresponding particle size distribution and the digital photograph of transparent dispersion of mono-dispersed $ZrO_2:Yb^{3+}/Er^{3+}$ nanocrystals with a solid content of 1 wt% (C) prepared with C12 modification in the benzyl alcohol-water system; Upconversion luminescence spectrum of $ZrO_2:Yb^{3+}/Er^{3+}$ nanophosphors (D), and energy level diagram of Yb^{3+} and Er^{3+} ions and the probable upconversion mechanism (E), under the excitation of 980 nm light.

than { −1 1 1 } planes of monoclinic ZrO_2 nanocrystals (m{ −1 1 1}). Corresponding to this, the bidentate configuration (COOad2 and COOHad2) has significantly higher adsorption energies, and consequently possesses a higher probability binding to planes than the monodentate configuration (COOad1 and COOHad1) (Fig. 7B and the corresponding table). As for the monoclinic situation, the bidentate configuration (COOad2) shows modest level of preferential affinity to m{ −1 1 1}, compared with the tetragonal counterpart (Fig. S5 and the corresponding first column of Table 1). Considering that the bidentate configuration consumes less surfactants than the monodentate one for particle protection, the difference of ligand coverage fashion between the two crystal forms validates the reason why monoclinic ZrO_2 requires more surfactants than tetragonal ZrO_2. Based on the above analysis, we find that the adsorption of surfactants onto t{1 0 1} is highly stable, since the adsorption energies of surfactants on m{ −1 1 1} are smaller than those on t{1 0 1}. Anisotropic growth is suppressed on tetragonal ZrO_2, as the ligand coverage is sufficient and stable. This explains why the monoclinic ZrO_2 nanocrystals display elongated shapes while the tetragonal-containing ZrO_2 nanocrystals display nearly "round" shapes.

Fig. 8 gives the digital photographs of monodispersed ZrO_2 nanocrystals with different solid contents and in different solvents. Sufficiency of surface modification prevented the nanoparticles from suffering secondary agglomeration in the courses of concentration and dilution. For this reason, highly stable and transparent ZrO_2 nanodispersion was visually identical to pure solvent even when the solid content reached as high as 60 wt% (Fig. 8A). As evidenced in the literature [3,72,73], fatty acids functionalized nanoparticles had fine dispersibility in nonpolar solvents, such as CYH, toluene, THF, CHCl₃, n-C₇H₁₆ and MSO (60 ~ 90 °C), forming long-term stable and transparent nanodispersions (Fig. 8B).

ZrO_2 is considered as a potential host matrix for photosensitive materials owing to its intrinsic high refractive index (about 2.2 @ 589 nm) and low phonon energy (about 470 cm⁻¹) [74,75]. Hence,

monodispersed $ZrO_2:Yb^{3+}/Er^{3+}$ nanophosphors were further prepared by the addition of Yb^{3+} and Er^{3+} inorganic salts. Fig. 9A–C displays the TEM images, XRD pattern, corresponding particle size distribution and digital photograph of the as-prepared $ZrO_2:Yb^{3+}/Er^{3+}$ nanodispersions. Compared to the nanocrystals without doping (as shown in Figs. 1B, 5 and 1F), the differences were listed below: the morphology was changed from spindle-like to near spherical structure; the crystalline form was transferred from monoclinic to tetragonal phase; the average length was decreased from 11 nm to 4 nm and the particle size distribution also became more uniform. As a result of rare earth doping process, typical upconversion luminescence spectrum was observed in $ZrO_2:Yb^{3+}/Er^{3+}$ nanophosphors after 980 nm excitation, which is shown in Fig. 9D. There are two main visible emission bands, including strong red bands centered at 652 and 678 nm, and the relatively weak blue one centered at 486 nm, which are associated to the $^4F_{9/2} \rightarrow {}^4I_{15/2}$ and $^4F_{7/2} \rightarrow {}^4I_{15/2}$ transitions of Er^{3+} ions, respectively. The possible upconversion luminescence mechanism was proposed in accordance with previous studies [75] to explain the observed visible emission under the excitation of 980 nm, as described in the energy level diagrams of Yb^{3+} and Er^{3+} ions in Fig. 9E. Firstly, the pumping photons (980 nm) populate the immediate excited state ($^4I_{11/2}$) of Er^{3+} ions from the ground state ($^4I_{15/2}$), via the energy transfer process (ET) from Yb^{3+} to Er^{3+} and/or the ground state absorption (GSA) from Er^{3+} to Er^{3+} itself. Then part of excited electrons on the $^4I_{11/2}$ level continue to absorb energy and this population is promoted to $^4F_{7/2}$ level by the excited state absorption (ESA) from Er^{3+} to Er^{3+} itself and/or by the second-step ET from Yb^{3+} to Er^{3+}. After that, parts of electrons on the $^4F_{7/2}$ level populate the intermediate $^4I_{9/2}$ level, and other excited electrons on the $^4I_{11/2}$ level populate the $^4I_{13/2}$ level, by nonradiative relaxation (NR) process. Electrons on the $^4I_{13/2}$ level are further excited into $^4F_{9/2}$ level by ESA. Finally, the $^4F_{7/2}$ level undergoes radiative decay to produce blue emission (486 nm), and the $^4F_{9/2}$ level undergoes radiative decay to produce red emission (652 and 678 nm).

4. Conclusions

Monodispersed ZrO_2 nanocrystals with tunable shapes, sizes and crystal forms can be efficiently prepared via an aqueous-organic two-phase system. The as-prepared ZrO_2 nanocrystals can be readily dispersed in nonpolar solvents, forming long-term stable transparent nanodispersions. In the benzyl alcohol-water system, when the length of the hydrocarbon chain of capping agents increased from C10 to C22, the shape of ZrO_2 nanocrystals tended to vary from fusiform to spherical structures; the particle length decreased from 20 to 5 nm; and the crystal form gradually changed from monoclinic to tetragonal phase. In the n-C_7H_{16}-water the system, similar situation occurred by adjusting the surfactants except for the shape transition. Shorter chain ligands, lower polarity of organic solvents, and higher NaOH concentration can result in an elongated morphology, which was proved by the results based on the DFT calculations. Calculated surface coordination chemistry confirmed that the stabilized dispersion of monoclinic ZrO_2 requires more surfactants than tetragonal ZrO_2. Furthermore, this approach was also applied in the preparation of fluorescent $ZrO_2:Yb^{3+}/Er^{3+}$, promising for applications such as photodynamic therapy, photodetectors and near-infrared sensing.

Declaration of Competing Interest

The authors declare that they have no known competing financial interests or personal relationships that could have appeared to influence the work reported in this paper.

Acknowledgments

Appendix A. Supplementary data

Supplementary data to this article can be found online at https://doi.org/10.1016/j.cej.2020.124843.

References

[1] Z. Hens, Economical routes to colloidal nanocrystals, Science 348 (2015) 1211.

[2] C.R. Kagan, E. Lifshitz, E.H. Sargent, D.V. Talapin, Building devices from colloidal quantum dots, Science 353 (2016) aac5523.

[3] J. Zhang, S. Ohara, M. Umetsu, T. Naka, T. Adschiri, Colloidal ceria nanocrystals: A tailor-made crystal morphology in supercritical water, Adv. Mater. 19 (2007) 203–206.

[4] X. Wang, Y. Li, Monodisperse nanocrystals: general synthesis, assembly, and their applications, Chem. Commun. 28 (2007) 2901–2910.

[5] L. Zhang, J. Yang, X. Zhao, X. Xiao, F. Sun, X. Zuo, J. Nan, Small-molecule surface-modified bismuth-based semiconductors as a new class of visible-light-driven photocatalytic materials: Structure-dependent photocatalytic properties and photosensitization mechanism, Chem. Eng. J. 380 (2020) 122546.

[6] R. Fang, C. Miao, H. Mou, W. Xiao, Facile synthesis of Si@TiO2@rGO composite with sandwich-like nanostructure as superior performance anodes for lithium ion batteries, J. Alloy. Compd. 818 (2020) 152884.

[7] Y. Nie, W. Xiao, C. Miao, M. Xu, C. Wang, Effect of calcining oxygen pressure gradient on properties of LiNi$_{0.8}$Co$_{0.15}$Al$_{0.05}$O$_2$ cathode materials for lithium ion batteries, Electrochim. Acta 334 (2020) 135654.

[8] Z. Kou, C. Miao, P. Mei, Y. Zhang, X. Yan, Y. Jiang, W. Xiao, Enhancing the cycling stability of all-solid-state lithium-ion batteries assembled with Li$_{1.3}$Al$_{0.3}$Ti$_{1.7}$(PO$_4$)$_3$ solid electrolytes prepared from precursor solutions with appropriate pH values, Ceram. Int. (2019), https://doi.org/10.1016/j.ceramint.2019.12.229.

[9] C. Du, Y. Guo, Y. Guo, X.Q. Gong, G. Lu, Synthesis of a hollow structured core-shell Au@CeO$_2$-ZrO$_2$ nanocatalyst and its excellent catalytic performance, J. Mater. Chem. A 5 (2017) 5601–5611.

[10] T. Akune, Y. Morita, S. Shirakawa, K. Katagiri, K. Inumaru, ZrO$_2$ nanocrystals as catalyst for synthesis of dimethylcarbonate from methanol and carbon dioxide: catalytic activity and elucidation of active sites, Langmuir 34 (2018) 23–29.

[11] X. Yang, X. Yu, M. Lin, M. Ge, Y. Zhao, F. Wang, Interface effect of mixed phase Pt/ZrO$_2$ catalysts for HCHO oxidation at ambient temperature, J. Mater. Chem. A 5 (2017) 13799–13806.

[12] Y. Zhang, Y. Zhao, T. Otroshchenko, H. Lund, M.M. Pohl, U. Rodemerck, D. Linke, H. Jiao, G. Jiang, E.V. Kondratenko, Control of coordinatively unsaturated Zr sites in ZrO$_2$ for efficient C-H bond activation, Nat. Commun. 9 (2018) 3794.

[13] J. Ke, F. He, J. Ye, Enhancing the bioactivity of yttria-stabilized tetragonal zirconia ceramics via grain-boundary activation, ACS Appl. Mater. Inter. 9 (2017) 16015–16025.

[14] D.A. Siddiqui, S. Sridhar, F. Wang, J.J. Jacob, D.C. Rodrigues, Can oral bacteria and mechanical fatigue degrade zirconia dental implants in vitro? ACS Biomater. Sci. Eng. 5 (2019) 2821–2833.

[15] E.K. Koehler, The structure and properties of refractory zirconia ceramics III. Studies of technical properties of materials and technological elaborations: a review of research works carried out in the USSR, Ceram. Int. 11 (1985) 3–12.

[16] J. Müller, T.S. Böscke, U. Schröder, S. Mueller, D. Bräuhaus, U. Böttger, L. Frey, T. Mikolajick, Ferroelectricity in simple binary ZrO$_2$ and HfO$_2$, Nano Lett. 12 (2012) 4318–4323.

[17] C.L. Tsai, G.S. Liou, Highly transparent and flexible polyimide/ZrO$_2$ nanocomposite optical films with a tunable refractive index and Abbe number, Chem. Commun. 51 (2015) 13523–13526.

[18] G. Ramírez-García, E. Díaz Cervantes, O. Mounzer, E. De la Rosa, T. López Luke, F.N. de la Cruz, A turn-on luminescence method for phosphate determination based on fast green-functionalized ZrO$_2$:Yb, Er@ZrO2 core@shell upconversion nanoparticles, Anal. Chem. 91 (2019) 14657–14665.

[19] Y.N. Ko, S.H. Choi, Y.C. Kang, S.B. Park, Electrochemical properties of ZrO$_2$-doped V$_2$O$_5$ amorphous powders with spherical shape and fine size, ACS Appl. Mater. Inter. 5 (2013) 3234–3240.

[20] K.D. Hristovski, P.K. Westerhoff, J.C. Crittenden, L.W. Olson, Arsenate removal by nanostructured ZrO$_2$ spheres, Environ. Sci. Technol. 42 (2008) 3786–3790.

[21] H. Wang, Y. Duan, W. Zhong, ZrO$_2$ nanofiber as a versatile tool for protein analysis, ACS Appl. Mater. Inter. 7 (2015) 26414–26420.

[22] K. Li, J.G. Chen, CO$_2$ hydrogenation to methanol over ZrO$_2$-containing catalysts: insights into ZrO$_2$ induced synergy, ACS Catal. 9 (2019) 7840–7861.

[23] J. Zhu, S. Albertsma, J.G. van Ommen, L. Lefferts, Role of surface defects in activation of O$_2$ and N$_2$O on ZrO$_2$ and yttrium-stabilized ZrO$_2$, J. Phys. Chem. B 109 (2005) 9550–9555.

[24] H. Wang, H. Chen, B. Ni, K. Wang, T. He, Y. Wu, X. Wang, Mesoporous ZrO$_2$ nanoframes for biomass upgrading, ACS Appl. Mater. Inter. 9 (2017) 26897–26906.

[25] A. Iribarren, G. Rodríguez-Gattorno, J.A. Ascencio, A. Medina, E. Torres-García, Tailoring chemical hardness in WO$_x$-ZrO$_2$ system, Chem. Mater. 18 (2006) 5446–5452.

[26] G. Liu, J. Li, K. Chen, H. Zhou, C. Pereira, J. Ferreira, Polycrystalline ZrN$_{1-x}$C$_x$ layers with (111) preferred orientation prepared by the carbothermal nitridation of ZrO$_2$ ceramics, Cryst. Growth Des. 9 (2009) 562–568.

[27] C. Liu, T.J. Hajagos, D. Chen, Y. Chen, D. Kishpaugh, Q. Pei, Efficient one-pot synthesis of colloidal zirconium oxide nanoparticles for high-refractive-index nanocomposites, ACS Appl. Mater. Inter. 8 (2016).

[28] P.T. Chung, S.H. Chiou, C.Y. Tseng, A.S.T. Chiang, Preparation and Evaluation of a Zirconia/Oligosiloxane Nanocomposite for LED Encapsulation, ACS Appl. Mater. Inter. 8 (2016) 9986–9993.

[29] K. De Keukeleere, J. De Roo, P. Lommens, J.C. Martins, P. Van Der Voort, I. Van Driessche, Fast and tunable synthesis of ZrO$_2$ nanocrystals: mechanistic insights into precursor dependence, Inorg. Chem. 54 (2015) 3469–3476.

[30] G. Garnweitner, L.M. Goldenberg, O.V. Sakhno, M. Antonietti, M. Niederberger, J. Stumpe, Large-scale synthesis of organophilic zirconia nanoparticles and their application in organic-inorganic nanocomposites for efficient volume holography, Small 3 (2007) 1626–1632.

[31] S. Zhou, G. Garnweitner, M. Niederberger, M. Antonietti, Dispersion behavior of zirconia nanocrystals and their surface functionalization with vinyl group-containing ligands, Langmuir 23 (2007) 9178–9187.

[32] K. Luo, S. Zhou, L. Wu, G. Gu, Dispersion and functionalization of nonaqueous synthesized zirconia nanocrystals via attachment of silane coupling agents, Langmuir 24 (2008) 11497–11505.

[33] X. Xu, X. Wang, Fine tuning of the sizes and phases of ZrO$_2$ nanocrystals, Nano Res. 2 (2009) 891–902.

[34] T. Ninjbadgar, G. Garnweitner, A. Boerger, L.M. Goldenberg, O. Sakhno, J. Stumpe, Synthesis of luminescent ZrO$_2$:Eu^{3+} nanoparticles and their holographic sub-micrometer patterning in polymer composites, Adv. Funct. Mater. 19 (2009) 1819–1825.

[35] A. Lauria, I. Villa, M. Fasoli, M. Niederberger, A. Vedda, Multifunctional role of rare earth doping in optical materials: nonaqueous sol-gel synthesis of stabilized cubic HfO$_2$ luminescent nanoparticles, ACS Nano 7 (2013) 7041–7052.

[36] N. Zhao, D. Pan, W. Nie, X. Ji, Two-phase synthesis of shape-controlled colloidal zirconia nanocrystals and their characterization, J. Am. Chem. Soc. 128 (2006) 10118–10124.

[37] W. Li, H. Huang, H. Li, W. Zhang, H. Liu, Facile synthesis of pure monoclinic and tetragonal zirconia nanoparticles and their phase effects on the behavior of supported molybdena catalysts for methanol-selective oxidation, Langmuir 24 (2008) 8358–8366.

[38] Y. Xia, C. Zhang, J.X. Wang, D. Wang, X.F. Zeng, J.F. Chen, Synthesis of transparent aqueous ZrO$_2$ nanodispersion with a controllable crystalline phase without modification for a high-refractive-index nanocomposite film, Langmuir 34 (2018) 6806–6813.

[39] K. Sato, H. Abe, S. Ohara, Selective Growth of Monoclinic and Tetragonal Zirconia Nanocrystals, J. Am. Chem. Soc. 132 (2010) 2538–2539.

[40] R.L. Penn, Imperfect oriented attachment: Dislocation generation in defect-free nanocrystals, Science 281 (1998) 969–971.

[41] S.M. Lee, S.N. Cho, J. Cheon, Anisotropic Shape Control of Colloidal Inorganic Nanocrystals, Adv. Mater. 15 (2010) 441–444.

[42] A. Tao, S. Habas, P. Yang, Shape control of colloidal metal nanocrystals, Small 4 (2008) 310–325.

[43] C. Ricolleau, L. Audinet, M. Gandais, T. Gacoin, Structural transformations in II-VI semiconductor nanocrystals, Eur. Phys. J. D. 9 (1999) 565–570.

[44] M. Klokkenburg, A.J. Houtepen, R. Koole, J.W.J. de Folter, B.H. Erné, E. van Faassen, D. Vanmaekelbergh, Dipolar structures in colloidal dispersions of PbSe and CdSe quantum dots, Nano Lett. 7 (2007) 2931–2936.

[45] W. Wang, S. Banerjee, S. Jia, M.L. Steigerwald, I.P. Herman, Ligand control of growth, morphology, and capping structure of colloidal CdSe nanorods, Chem. Mater. 19 (2007) 2573–2580.

[46] X. Peng, Mechanisms for the shape-control and shape-evolution of colloidal semi-conductor nanocrystals, Adv. Mater. 15 (2003) 459–463.

[47] P.D. Cozzoli, A.A. Kornowski, H. Weller, Low-temperature synthesis of soluble and processable organic-capped anatase TiO$_2$ nanorods, J. Am. Chem. Soc. 125 (2003) 14539–14548.

[48] H. Yao, Y. Wang, J. Yu, G. Luo, Ultrafast, continuous and shape-controlled pre-paration of CeO$_2$ nanostructures: nanorods and nanocubes in a microfluidic system, Ind. Eng. Chem. Res. 57 (2018) 7525–7532.

[49] C.H. Ho, C.P. Tsai, C.C. Chung, C.Y. Tsai, C.H. Lai, Shape-controlled growth and shape-dependent cation site occupancy of monodisperse Fe$_3$O$_4$ nanoparticles, Chem. Mater. 23 (2011) 1753–1760.

[50] M.L. Kahn, M. Monge, V. Collière, F. Senocq, A. Maisonnat, B. Chaudret, Size- and shape-control of crystalline zinc oxide nanoparticles: a new organometallic syn-thetic method, Adv. Funct. Mater. 15 (2005) 458–468.

[51] K. Srigurunathan, R. Meenambal, A. Guleria, D. Kumar, J.M.D.F. Ferreira, S. Kannan, Unveiling the effects of rare-earth substitutions on the structure, me-chanical, optical, and imaging features of ZrO$_2$ for biomedical applications, ACS Biomater. Sci. Eng. 5 (2019) 1725–1743.

[52] J. Zhou, R. Lei, H. Wang, C. Chen, B. Chen, E. Pan, S. Zhao, S. Xu, Er^{3+}/Yb^{3+}-codoped ZrO$_2$ nanocrystals as ratiometric luminescence nanothermometers that cover three biological windows, ACS Appl. Nano Mater. 3 (2020) 186–194.

[53] C. Liu, B. Liu, J. Zhao, Z. Di, D. Chen, Z. Gu, L. Li, Y. Zhao, Nd^{3+}-sensitized up-conversion metal-organic frameworks for mitochondria-targeted amplified photo-dynamic therapy, Angew. Chem. Int. Edit. 59 (2020) 1–6.

[54] Q. Wang, Q. Zhao, X. Zhao, Y.J. Zheng, J. Wang, X. Luo, J. Dan, R. Zhu, Q. Liang, L. Zhang, P.K.J. Wong, X. He, Y.L. Huang, X. Wang, S.J. Pennycook, G. Eda, A.T.S. Wee, High-energy gain upconversion in monolayer tungsten disulfide pho-todetectors, Nano Lett. 19 (2019) 5595–5603.

[55] H. Tachibana, N. Aizawa, Y. Hidaka, T. Yasuda, Tunable full-color electro-luminescence from all-organic optical upconversion devices by near-infrared sen-sing, ACS Photon. 4 (2017) 223–227.

[56] S.W. Cao, Y.J. Zhu, Monodisperse α-Fe$_2$O$_3$ mesoporous microspheres: one-step NaCl-assisted microwave-solvothermal preparation, size control and photocatalytic property, Nanoscale Res. Lett. 6 (2011) 1.

[57] Y. Xia, Q. Sun, D. Wang, X.F. Zeng, J.X. Wang, J.F. Chen, Surfactant-free aqueous dispersions of shape- and size-controlled zirconia colloidal nanocrystal clusters with enhanced photocatalytic activity, Langmuir 35 (2019) 11755–11763.

[58] Y. Wang, H. Gao, Influence of a ZrO$_2$ support and its surface structures on the stability and nucleation of Pt$_n$ (n = 1–5) clusters: a density functional theory study, J. Phys. Chem. B 121 (2017) 2132–2141.

[59] D. Liu, X. Xu, Y. Du, X. Qin, Y. Zhang, C. Ma, S. Wen, W. Ren, E.M. Goldys, J.A. Piper, Three-dimensional controlled growth of monodisperse sub-50 nm het-erogeneous nanocrystals, Nat. Commun. 7 (2016) 10254.

[60] Y. Sui, T. Ke, Q. Tian, S. Kang, Interaction between Y^{3+} and oleate ions for the cubic-to-hexagonal phase transformation of NaYF$_4$ nanocrystals, J. Phys. Chem. C 116 (2012) 1732–1739.

[61] G. Kresse, J. Furthmüller, Efficient iterative schemes for Ab initio total-energy calculations using a plane-wave basis set, Phys. Rev. B 54 (1996) 11169.

[62] J. Perdew, K. Burke, M. Ernzerhof, Generalized gradient approximation made simple, Phys. Rev. Lett. 77 (1996) 3865–3868.

[63] Y. Zhang, W. Yang, Comment on "generalized gradient approximation made simple", Phys. Rev. Lett. 80 (1998) 890.

[64] M. Dion, H. Rydberg, E. Schroder, D.C. Langreth, B.I. Lundqvist, Vander waals density functional for general geometries, Phys. Rev. Lett. 92 (2004) 246401.

[65] Y. Yadong, A.A. Paul, Colloidal nanocrystal synthesis and the organic-inorganic interface, Nature 437 (2005) 664–670.

[66] G. Pacchioni, Ketonization of carboxylic acids in biomass conversion over TiO$_2$ and ZrO$_2$ surfaces: a DFT perspective, ACS Catal. 4 (2014) 2874–2888.

[67] A. Chen, Y. Zhou, S. Miao, Y. Li, W. Shen, Assembly of monoclinic ZrO$_2$ nanorods: formation mechanism and crystal phase control, CrystEngComm 18 (2016) 580–587.

[68] X.J. Huang, X.F. Zeng, J.X. Wang, L.L. Zhang, J.F. Chen, Synthesis of monodispersed ZnO@SiO$_2$ nanoparticles for anti-UV aging application in highly transparent polymer-based nanocomposites, J. Mater. Sci. 54 (2019) 8581–8590.

[69] H. Chen, X. Tian, L. Jing, Unsaturated polyester resin nanocomposites containing ZnO modified with oleic acid activated by N N-carbonyldiimidazole, Polymers 10 (2018) 362–375.

[70] G. Garnweitner, L.M. Goldenberg, O.V. Sakhno, M. Antonietti, M. Niederberger, J. Stumpe, Large-scale synthesis of organophilic zirconia nanoparticles and their application in organic-inorganic nanocomposites for efficient volume holography, Small 3 (2010) 1626–1632.

[71] D. Pan, G. Xu, J. Wan, Z. Shi, M. Han, G. Wang, Tuning the solubility of TiO$_2$ nanoparticles in apolar solvents by doping with Co^{2+}, Langmuir 22 (2006) 5537–5540.

[72] Z. Hens, J.C. Martins, A solution nmr toolbox for characterizing the surface chemistry of colloidal nanocrystals, Chem. Mater. 25 (2013) 1211–1221.

[73] N. Pinna, S. Grancharov, P. Beato, P. Bonville, M. Antonietti, M. Niederberger, Magnetite nanocrystals: Nonaqueous synthesis, characterization, and solubility, Chem. Mater. 17 (2005) 3044–3049.

[74] T. López-Luke, E. De la Rosa, P. Salas, C. Angeles-Chavez, L.A. Díaz-Torres, S. Bribiesca, Enhancing the up-conversion emission of ZrO$_2$:Er^{3+} nanocrystals prepared by a micelle process, J. Phys. Chem. C 111 (2007) 17110–17117.

[75] X. Qu, H. Song, X. Bai, G. Pan, B. Dong, H. Zhao, F. Wang, R. Qin, Preparation and upconversion luminescence of three-dimensionally ordered macroporous ZrO$_2$: Er^{3+}, Yb^{3+}, Inorg. Chem. 47 (2008) 9654–9659.